Journal of Dynamics, Monitoring and Diagnostics, 2024, 3, 180-189
https://doi.org/10.37965/jdmd.2024.567

ISTP
RESEARCH ARTICLE

MAPOD Analysis in Eddy Current Testing of Flaws Considering Multiple Response Signals and Multiple Flaw Parameters

Shixi Yang,[1,2] Liping Zhang,[1,2] Xiwen Gu,[1,2] and Weidi Huang[1,2]
[1]State Key Laboratory of Fluid Power & Mechatronic Systems, Zhejiang University, Hangzhou 310058, China
[2]School of Mechanical Engineering, Zhejiang University, Hangzhou 310058, China

(Received 11 June 2024; Revised 15 July 2024; Accepted 07 August 2024; Published online 10 August 2024)

Abstract: The reliability of the eddy current testing (ECT) in flaw detection is quantitatively evaluated by the probability of detection (POD). Precise and efficient modeling of POD gives direction for the implement of ECT on sites to avoid false or missing flaw detection. Traditional POD analysis focuses on single uncertain factor or single response signal with limited credibility in engineering. This paper considers multiple response signals and multiple flaw parameters to perform POD. The flaw length, the flaw depth, the coil impedance, and the magnetic flux density are comprehensively studied under various lift-off distances. A finite element model (FEM) of ECT is established and verified with experiments to obtain sufficient simulation data for discrete POD modeling. The continuous POD function is then fitted based on the discrete values to show the superiority of integrating multiple factors. A comparison with conventional POD analysis further demonstrates the higher reliability of ECT flaw detection considering multiple flaw parameters and multiple response signals, especially for small flaws.

Keywords: Eddy current testing; finite element model; multiple response signals; probability of detection

I. INTRODUCTION

The eddy current testing (ECT) has been widely applied to detect crack flaws of metal material to ensure structural integrity [1]. However, detection uncertainty usually occurs during the detection process in the case of misdetections or false alarms, as there are a lot of factors largely polluting the eddy current signals, such as surface roughness [2], nonuniform electromagnetic properties [3], and variant lift-off distances [4]. It is essential to determine the probability that a flaw with a specific dimension would be detected or missed. This brings a typical research topic of ECT and other nondestructive testing (NDT) techniques—probability of detection (POD) analysis, to evaluate the reliability of flaw detection results.

The primary idea behind the POD analysis is to use a probabilistic function, POD(a), to indicate the likelihood that a flaw with a size of a will be detected [5]. NASA firstly employed a binomial distribution to determine the sensitivity and reliability of the NDT results on metallic materials [6]. Later on, the aircraft industry contributed to the majority of the pioneering works of POD research, especially in the detection of fatigue cracks [7]. Nowadays, POD analysis has been widely applied to assess the detection capability in various scenarios, such as early warning of debris flow in nature [8], ultrasonic detection of railway hollow axle cracks [9], and weld joints inspection by various NDT methods in the hydroelectric turbine [10].

POD analysis has been proved a useful way to assess how well an ECT or other NDT approaches perform toward flaw detection. Traditional POD analysis requires a large volume of experimental data to statistically determine the parameters of the probabilistic function [11,12]. Sufficient number of machine-made flaw samples and repeated experiments are necessary to obtain the statistical results of the POD curve, which is time-consuming and expensive. With recent developments in computers and computational physics, model-assisted POD (MAPOD) analysis represents a growing field with numerical or theoretical simulations replacing parts or all of the experimental measurements to construct a POD curve [13]. Rosell *et al.* [14] established a fatigue crack model in titanium plates by finite element analysis, and then MAPOD curve was built using numerical computations. Du *et al.* [15] generated sufficient numerical data by a kriging metamodel to construct the MAPOD curve and achieved high-efficiency uncertainty analysis for the ultrasonic defect detection. For the flaw detection using ECT, experimental data is usually combined with finite element modeling data to calculate the POD curves [16].

The quality of the constructed probabilistic function POD(a) ensures the evaluation effectiveness of ECT. Conventional MAPOD analysis of ECT only consider the effect of single flaw parameter on single response signal. For example, Yang [17] considered the changes of coil impedance under different flaw lengths to establish the POD curve. Flaw depth could also affect the POD, as proved by Yusa [18]. This implies that multiple flaw parameters are necessary to make a more reliable MAPOD analysis [19,20]. Tomizawa *et al.* [21] pointed out that multiple features abstracted from response signals can contain more essential information to distinguish signals caused by flaws and noise. Baskaran *et al.* [22] showed that MAPOD analysis with single flaw parameter (flaw length) and multiple response signal features (the maximum change in coil impedance at two different frequencies) is more reliable, especially for larger flaws. Both the multiple flaw parameters (flaw length and flaw depth) and multiple response signal features (the maximum change in the magnetic flux density of three directional components) were considered when constructing MAPOD in another

Corresponding author: Xiwen Gu (e-mail: guxw@zju.edu.cn).

work of them [23]. However, the multiple response signals used in these studies are essentially homologous.

ECT works on the principle of electromagnetic induction. The coil impedance signal represents the changes in the electric field, while the magnetic flux density signal shows the changes in the magnetic field. Features extracted from multi-sensor signals have been proved to perform better in fault diagnosis [24,25]. It inspires us to explore the performance of using multi-sensor signals in ECT of flaw detection. There are two main questions worth studying: (1) Whether the detection reliability would further improve considering both the electric-related and magnetic-related signals? (2) Which signal is more sensitive to the flaw considering both the flaw length and depth?

MAPOD analysis considering multiple response signals and multiple flaw parameters (2M-MAPOD) is carried out in this paper to evaluate the reliability of ECT toward rectangular opening crack. The multiple response signals, the coil impedance and the magnetic flux density, are for the first time integrated to build the MAPOD model toward multiple flaw parameters (flaw length and flaw depth). The response signals are obtained from a finite element model (FEM) with normally distributed lift-off distance to perform MAPOD analysis. The flaw detection probability of ECT using two heterogenic signals is studied to find the minimum detectable flaw size. Correlation between the response signals and multiple flaw parameters is captured.

This paper consists of 5 sections. In section II, the overall framework and details of the proposed 2M-MAPOD are introduced. The effectiveness of the FEM is verified by an experiment, and the 2M-MAPOD analysis is carried out using the simulation data in section III. In section IV, the proposed 2M-MAPOD are compared with those considering multiple response signals and single flaw parameter, single response signal and multiple flaw parameters, and single response signal and single flaw parameter. In the last section, we conclude this work with possible future outlooks and also limitations.

II. THE FRAMEWORK OF THE PROPOSED 2M-MAPOD ANALYSIS

Figure 1 illustrates the process of the proposed 2M-MAPOD analysis.

Uncertainty factors influencing the ECT results are firstly analyzed. The lift-off distance is considered the most sensitive factor bringing the measurement imperfection. It is modeled as a normal distribution and sampled by Latin hypercube sampling (LHS) method. The FEM is established considering the lift-off variances. Numerical simulations are carried out to acquire the features of multiple response signals considering a flaw with various length L_{flaw} and depth D_{flaw}. The response signal features are the peak values of the coil impedance and the magnetic flux density corresponding to F_1 (Ω) and F_2 (μT), respectively. After validating the multivariate normality of the two response signal features, the discrete POD values can be gained by computing POD considering multiple flaw parameters and multiple response signal features. Finally, the generalized logistic function (GLF) regression is implemented to obtain the continuous POD function.

A. FINITE ELEMENT ANALYSIS

Maxwell's equations are commonly used to describe electromagnetic eddy current physical models. The $\boldsymbol{A}-V$ formulation is employed using the magnetic vector potential $\boldsymbol{A}$ and the electric scalar potential V [26]. In the FEM, the electromagnetic fields are computed using the differential equation [27]:

$$\nabla\left(\times\frac{1}{\mu}\nabla\times\boldsymbol{A}\right)+\sigma(\mathrm{j}\omega\boldsymbol{A}+\nabla V)=\boldsymbol{J}_{\mathrm{s}} \tag{1}$$

where $\boldsymbol{J}_{\mathrm{s}}$ is the source current density, μ is the magnetic permeability, ω is the angular frequency, and σ is the electrical conductivity. The displacement current is ignored assuming that the induced and source currents predominate.

The magnetic flux density in the finite element analysis is presented as [28]:

$$\boldsymbol{B}=\nabla\times\boldsymbol{A} \tag{2}$$

The change in the impedance is computed considering the conductivity of the conductor in the unflawed region and the conductivity of the air in the flawed region:

$$\Delta Z=Z_{\text{flawed}}-Z_{\text{unflawed}}=\Delta X+\Delta R \tag{3}$$

where ΔX is the change in reactance and ΔR is the change in resistance. ΔX and ΔR can be calculated by [29]:

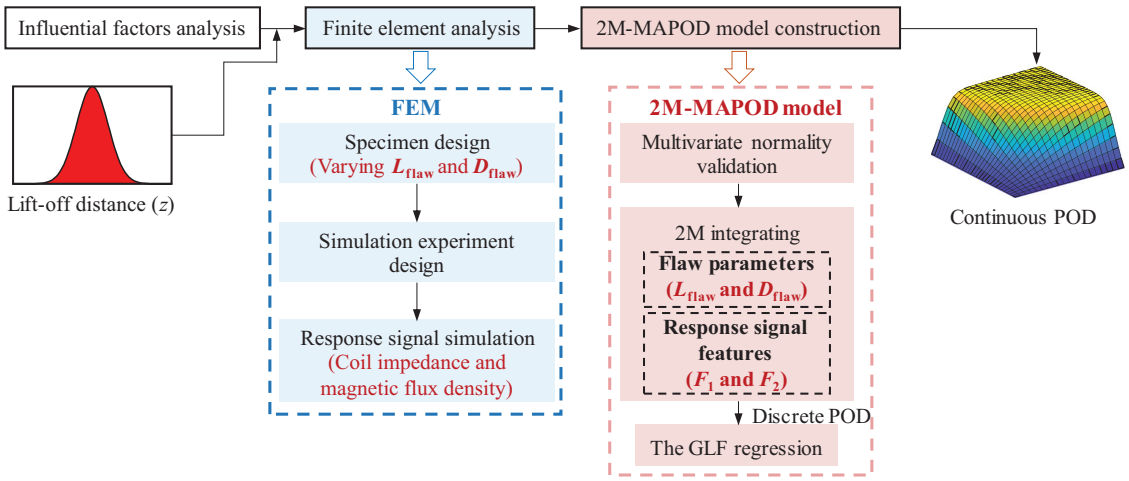

Fig. 1. The framework of the 2M-MAPOD analysis proposed in this study.

$$\Delta X=\frac{2\pi f}{I^2}\left[\iiint \boldsymbol{H}_{\text{flawed}}\cdot\boldsymbol{B}^*_{\text{flawed}}\mathrm{d}\Gamma-\iiint \boldsymbol{H}_{\text{unflawed}}\cdot\boldsymbol{B}^*_{\text{unflawed}}\mathrm{d}\Gamma\right] \tag{4}$$

$$\Delta R=\frac{1}{I^2}\left[\iiint \boldsymbol{J}_{\text{i,flawed}}\cdot\boldsymbol{E}^*_{\text{flawed}}\mathrm{d}\Gamma_f-\iiint \boldsymbol{J}_{\text{i,unflawed}}\cdot\boldsymbol{E}^*_{\text{unflawed}}\mathrm{d}\Gamma_f\right] \tag{5}$$

where $\boldsymbol{H}$ represents the magnetic field, $\boldsymbol{B}^*$ is the complex conjugate of the magnetic flux density, and $\boldsymbol{J}_{\text{i}}$ is the induced current density. $\boldsymbol{E}^*$ represents the complex conjugate of the electric field. Γ_f is the volume of the conductor and flaw domains, and Γ is the entire volume of all domains.

In this work, the FEM is established on an aluminum plate with a narrow opening surface flaw. All simulations are carried out with COMSOL using second-order vector and nodal basis functions to describe the magnetic vector potential and electric scalar potential separately. Outer boundary is set to be infinite element field to ensure sufficient distance between the positions of the outer boundaries and any source. The FEM is used to get the response signals toward a given flaw.

B. 2M-MAPOD MODEL CONSTRUCTION

The coil is located at a lift-off distance z, and the variation of z is assumed to be normally distributed with a mean of μ mm and a standard deviation of σ mm [30]:

$$z\sim \mathrm{N}(\mu,\sigma^2) \tag{6}$$

M different flaw lengths and N different flaw depths are taken into consideration for the POD construction. All the flaw lengths are designated as $L_1, L_2, \cdots, L_{\mathrm{M}}$, and all the flaw depths are designated as $D_1, D_2, \cdots, D_{\mathrm{N}}$. For each set of the flaw parameters $\{L_i, D_j\}$, the lift-off distances of sample size K are generated through LHS based on equation (6). Then each response signal feature with a sample size of K is obtained. The set of features are expressed as $\{F_1, F_2\}\in F$ where F_1 is the peak value of coil impedance and F_2 is the peak value of magnetic flux density.

With the assumption of normal distribution of z, the feature distribution F can be modeled as:

$$p(F|L_{\text{flaw}}=L_i, D_{\text{flaw}}=D_j)\sim \mathrm{N}(\hat{\mu},\hat{K}) \tag{7}$$

where the mean $\hat{\mu}=[\mu_1,\mu_2]\in \mathrm{R}^{2\times 2}$. The covariance $\hat{K}=\begin{bmatrix}\sigma_1{}^2 & \rho_1\sigma_1\sigma_2\\ \rho_1\sigma_1\sigma_2 & \sigma_2{}^2\end{bmatrix}\in \mathrm{R}^{2\times 2}$, denoted with a circumflex hat, can be estimated from the FEM data with a sample size of K. Mardia's multivariate skewness and kurtosis test [31] is implemented to testify the multivariate normality of the response signal features.

The POD for a given pair of flaw parameters is calculated as:

$$Pod\left(F|L_{\text{flaw}}=L_i, D_{\text{flaw}}=D_j\right)=\int_{F_2^{\text{th}}}^{\infty}\int_{F_1^{\text{th}}}^{\infty} p\left(L_i,D_j\right)\mathrm{d}F_1\mathrm{d}F_2 \tag{8}$$

where F_1^{th} and F_2^{th} correspond to the threshold levels for each of the two response signal features. The threshold values are determined from the response signals when the probe is moved over the plate in an unflawed region.

Equation (8) yields a discrete form of the POD curve. To obtain a continuous function, the discrete values can be connected to a form of the GLF denoted as:

$$f(L_i,D_j|\Theta)=\alpha_{\text{p}}/\left\{1+\chi.\mathrm{e}^{-[\beta_{\text{p}}(L_i-\gamma_{\text{p}})+\delta_{\text{p}}(D_j-\varepsilon_{\text{p}})]\eta_{\text{p}}}\right\} \tag{9}$$

where parameter $\chi=\mathrm{e}^{[\varsigma_{\text{p}}(L_i-\gamma_{\text{p}})(D_j-\varepsilon_{\text{p}})]}$ is related to the cross-correlation between the flaw length and depth. α_{p} represents the upper asymptote of the function. γ_{p} and ε_{p} are shifts along the L_{flaw} and D_{flaw} directions. β_{p} and δ_{p} correspond to the weights associated with L_{flaw} and D_{flaw}. Θ is the collective set of all the parameters in equation (9), that is, $\Theta=[\alpha_{\text{p}},\beta_{\text{p}},\gamma_{\text{p}},\delta_{\text{p}},\varepsilon_{\text{p}},\eta_{\text{p}},\varsigma_{\text{p}}]$.

To estimate the unknown parameters Θ in equation (9), a residual function is created and the residual in the least squares approach is minimized as:

$$S(\Theta)=\sum_{i=1}^{M}\sum_{j=1}^{N}\frac{1}{2}[Pod(F|L_i,D_j)-f(L_i,D_j|\Theta)]^2,$$
$$\hat{\Theta}\in\underset{\Theta}{\operatorname{argmin}}S(\Theta) \tag{10}$$

The residual function is a nonlinear function hardly to obtain a closed-form solution. Levenberg–Marquardt (LM) algorithm, a widely used optimization algorithm, is adopted to estimate Θ [32]. Generating an initial guess ($\hat{\Theta}^k$), the parameter ($\hat{\Theta}^{k+1}$) is updated by descending the gradient. This parameter searching process is iterated until the difference of the residual sum of squares between two successive iterations stops improving (i.e., $\delta_k S(\Theta)\to 0$) or the number of iterations exceeds a certain value. The LM parameter update principle is given as:

$$\left[J_{\text{res}}{}^{\mathrm{T}}J_{\text{res}}+\wedge.\mathrm{diag}\left(J_{\text{res}}{}^{\mathrm{T}}J_{\text{res}}\right)\right]\left\{\hat{\Theta}^{k+1}-\hat{\Theta}^{k}\right\}=\left[J_{\text{res}}{}^{\mathrm{T}}R_{\text{res}}\right] \tag{11}$$

where $R_{\text{res}}=Pod(F|L_i,D_j)-f(L_i,D_j|\Theta)$. The Jacobian matrix J_{res} of R_{res} has a dimension of $(M\cdot N)\times 7$, $J_{\text{res}}=\left[\frac{\partial R_{\text{res}}}{\alpha_{\text{p}}},\frac{\partial R_{\text{res}}}{\beta_{\text{p}}},\frac{\partial R_{\text{res}}}{\gamma_{\text{p}}},\frac{\partial R_{\text{res}}}{\delta_{\text{p}}},\frac{\partial R_{\text{res}}}{\varepsilon_{\text{p}}},\frac{\partial R_{\text{res}}}{\eta_{\text{p}}},\frac{\partial R_{\text{res}}}{\varsigma_{\text{p}}}\right]$. The scalar $\wedge$, is the damping parameter. It determines the percentage of step change that can be updated along the gradient direction of the parameter. The term $\mathrm{diag}(J_{\text{res}}{}^{\mathrm{T}}J_{\text{res}})$ is a diagonal matrix containing the diagonal entries of $J_{\text{res}}{}^{\mathrm{T}}J_{\text{res}}$, which is one way to mitigate the consequences of parameter scaling. It represents an ellipsoidal trust region instead of a traditional spherical trust region that relies on an identity matrix in place of $\mathrm{diag}(J_{\text{res}}{}^{\mathrm{T}}J_{\text{res}})$.

III. 2M-MAPOD ANALYSIS

A. FEM CONSTRUCTION

Numerical simulations are conducted on flat plates made of aluminum using COMSOL Multiphysics 5.6 with the AC/DC module. The tangential components of the magnetic vector potential are set to zero. For the 3D electromagnetic field simulation, the gauge fixing for the magnetic vector potential should be added in the magnetic fields. The finite element mesh employs free tetrahedral mesh, and the mesh in the probe domain and the flaw domain is super-refined. The movement of the probe in the geometry is

achieved via a parametric sweep. The air conductivity is set to 0.1 for the convergence of the calculation.

The parameters used in simulations are presented in Fig. 2., and the corresponding values are listed in Table I. During simulation, the flaw length L_{flaw} is set to vary from 0.1 mm to 10 mm. The increment is 0.1 mm from 0.1 mm to 0.9 mm while from 1 mm to 10 mm, a larger increment of 1 mm is applied. Similarly, the flaw depth D_{flaw} includes 10 values. It manifests a rise step of 0.1 mm from 0.1 mm to 0.4 mm and another rise step of 0.5 mm from 0.5 mm to 3 mm. The flaw width W_{flaw} is fixed at 0.5 mm.

Hand-held eddy current probe with relatively small size is chosen in the simulation and also the experiments to ensure the flaw detection sensitivity. In real testing, the slight shake of the probe during movement and the roughness of the plate could bring uncertainty to the lift-off distance. The lift-off distance of the probe to the plate surface is set to fluctuate around 0.5 mm to prevent abrasion and ensure the detectability. The exciting frequency is chosen as 200 kHz based on the skin effect of the material so that the detection depth could reach 3 mm. Figure 3 displays the finite element simulation model.

The distribution of the magnetic flux density during probe movement is displayed in Fig. 4. The center of the coil has the highest magnetic flux density, and magnetic flux density aggregation occurs at the corners of the flaw

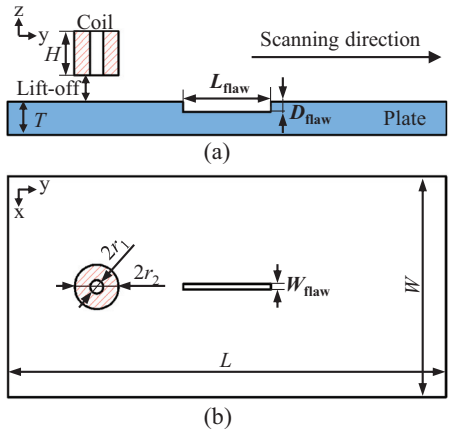

Fig. 2. Setup of parameters: (a) front view and (b) top view.

Table I. Parameter values in simulations

	Parameter	Value
Plate	Length L	200 mm
	Width W	100 mm
	Thickness T	5 mm
	Conductivity	3.557×10^{7} S/m
Flaw	L_{flaw}	0.1:0.1:0.9 mm and 1:1:10 mm
	W_{flaw}	0.5 mm
	D_{flaw}	0.1:0.1:0.4 mm and 0.5:0.5:3 mm
Coil	Inner radius r_1	1.487 mm
	Outer radius r_2	5 mm
	Height H	10 mm
	Turns number	325
	Lift-off	N(0.5,0.1) mm

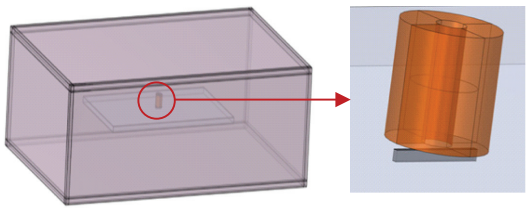

Fig. 3. Finite element simulation model.

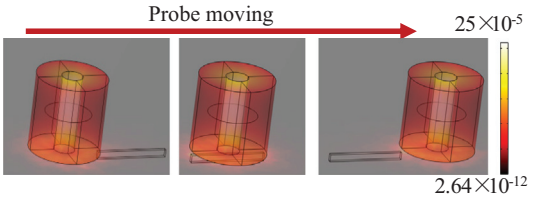

Fig. 4. Distribution of magnetic flux density during scanning.

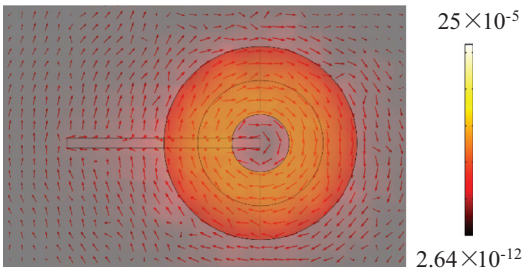

Fig. 5. Eddy current distribution when the flaw exists.

compared with unflawed region. Figure 5 exhibits the eddy current distribution in the specimen when the flaw exists. The red arrow represents the flow direction of the eddy current. When the eddy current touches the flaw, it flows along the flaw edge firstly and then continues to flow around the flaw. In the direction of flaw depth, the eddy currents deflect and flow from the bottom of the flaw.

LHS method is used to sample 200 times of lift-off distances. The peak values of the coil impedance F_1 and the magnetic flux density F_2 concerning a flaw are extracted as response signal features for all the lift-off distances. Take a flaw with a length of 10 mm and depth of 1 mm as an example, the scan results at a certain lift-off distance are shown in Fig. 6. The red asterisks are the points of the features $\{F_1, F_2\}$.

B. FEM VALIDATION

To verify the FEM, an ECT experimental system is built consisting of a numerical control (NC) platform, an eddy current instrument, a probe, and the specimens, as shown in Fig. 7. The NC platform is driven by the servo motors, which controls the xyz triaxial movement of the probe. The coil impedance of the response signal is collected by the eddy current instrument. The lift-off distance is determined with a feeler gauge of 0.5 mm thickness. Fifty repeated scans are performed to ensure sufficient changes of lift-off distance during measurement. Electrical discharge machining and wire cutting method are applied to fabricate rectangular defects [33]. Due to the limitations of electric

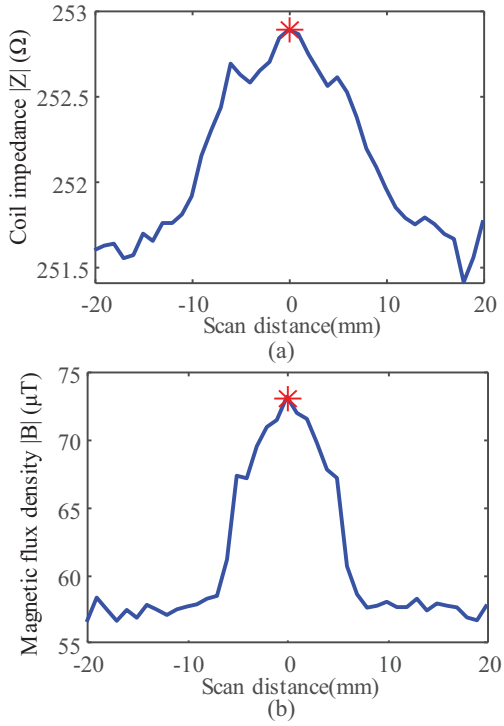

Fig. 6. An example of the flaw response signals: (a) coil impedance |Z| and (b) magnetic flux density |B|.

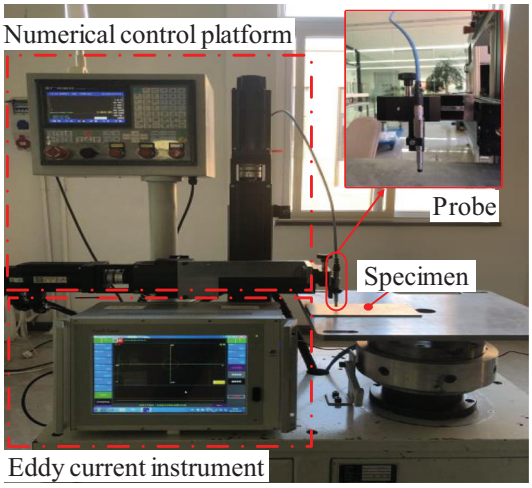

Fig. 7. Experiment setup.

discharge machining manufacturing, the flaw lengths on the plate are 1, 2, and 3 mm, and the corresponding depth increases from 0.5 to 2 mm with an increment of 0.5 mm. Besides, the flaw lengths of 0.2 mm and 0.5 mm can only be machined with depth of 0.5 and 1.0 mm.

After normalizing and averaging the results of 50 measurements, the response signal feature, the peak value of coil impedance (F_1), is gained. Comparison of the model simulated F_1 and experimental signals is illustrated in Fig. 8. Both of the values from simulation and experiments increase with the increasing flaw depth (Fig. 8(a)) or flaw length (Fig. 8(b)). The simulation values are slightly larger than the experimental values because the simulation environment is ideal without noise interference. The overall trend of simulation and experimental values is consistent. It

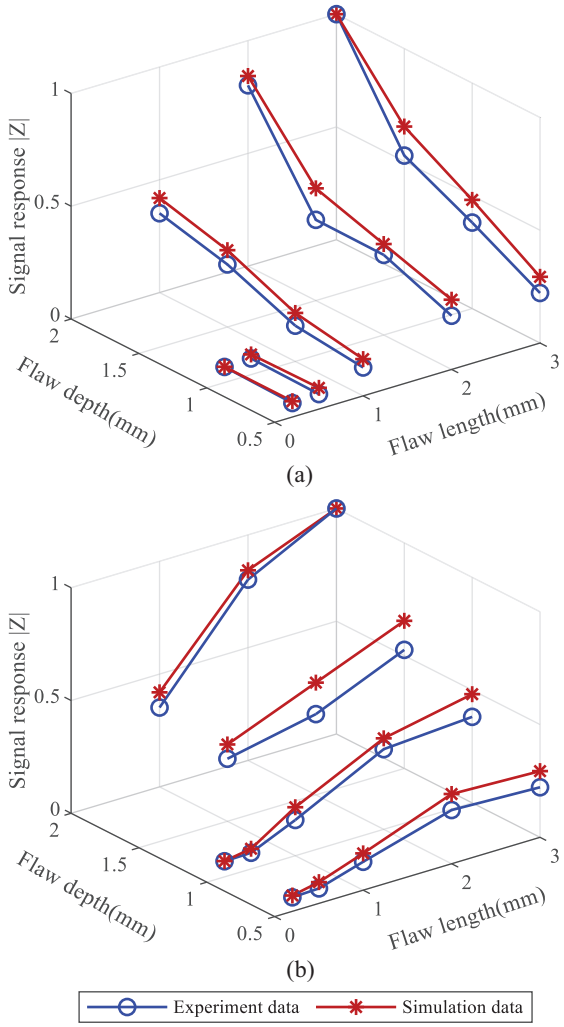

Fig. 8. Comparison of F1 between experiment and simulation: (a) depth direction and (b) length direction.

can be clearly seen in Fig. 8. that the ECT signal is affected by both the flaw length and flaw depth. In order to build a more reliable POD curve, two flaw parameters, flaw length and flaw depth, should be considered at the same time.

C. IMPLEMENTATION OF 2M-MAPOD

A multivariate normality test is carried out to verify the distribution normality of the two response signal features in simulation. The lift-off distance is distributed as N(0.5, 0.1). Taking a flaw with 10 mm length and 1 mm depth as an example, the Mardia's multivariate skewness and kurtosis test is implemented. The significance level is chosen as 0.05. The obtained P-values of the max kurtosis test are 0.6281 and 0.9169. The P-values are both greater than 0.05, meaning that there is no statistical evidence of the presence of skewness and kurtosis in the features. So the response signal features of the flaw with given parameters follow multivariate normal distribution.

Multivariate normal distribution can also be certified by the Q-Q plot concisely, as an example shown in Fig. 9. The horizontal axis is the value of the quantile of the chi-square distribution, while the vertical axis is the square of the Mahalanobis distance. The points in the scatter plot are directly opposite to the angular bisector of the xy axis,

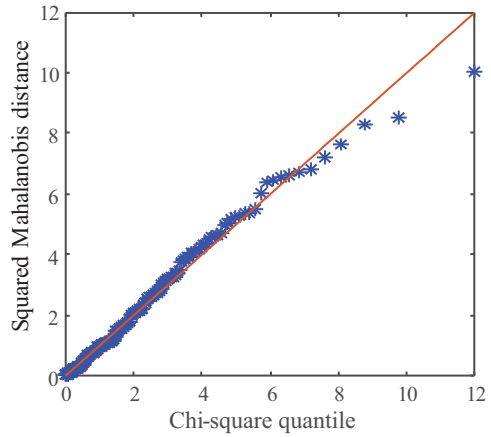

Fig. 9. Chi-square Q-Q plot of a flaw with 10 mm length and 1 mm depth.

indicating that the signal features conform to the binary normal distribution. Figure 10 displays an example of the distribution of the response signal features$\{F_1,F_2\}$ under various lift-off distances. The black dot represents the discrete points of $\{F_1,F_2\}$ when the lift-off distance changes. The solid line represents the contour of the probability density of the binary normal distribution.

The lift-off distance is sampled 200 times in simulation. For each of the lift-off distance, different pairs of flaw length and flaw depth are set to obtain the corresponding response signal features $\{F_1,F_2\}$ in the noise condition. The results are exhibited in Fig. 11. F_1 and F_2 both show high sensitively to the variation of the flaw parameters. They vary with the flaw length as well as the flaw depth, not just single flaw parameter. F_1 of the coil impedance keeps increasing rapidly with the increase in flaw length and depth. Differently, F_2 of the magnetic flux density grows quickly in the small value region, while the growing trend slows down when the flaw parameters getting larger. Considering the behavior distinction of F_1 and F_2 toward flaw parameters, the 2M-MAPOD analysis integrating multiple response signals could fuse more information in different aspects, thus improving the reliability of ECT.

The threshold values for F_1 and F_2 are decided from the noise. The coil is scanned in a flaw-free area over the plate for 500 times to obtain the corresponding signals. It is shown in Fig. 12 that the noise has a normal distribution. The mean value for F_1 is $\mu_1 = 252.0216\ \Omega$ and for F_2 is $\mu_2 = 58.4678\ \mu T$. The distribution of the standard deviation for the measured values, also called the measurement uncertainty, is determined by bootstrapping. Figure 13 represents the histogram of the standard deviation of the data points around the mean value at the two response signal features. The standard deviation for F_1 is $\sigma_1 = 0.4367\ \Omega$ and for F_2 $\sigma_2 = 1.4800\ \mu T$. The detection thresholds should be higher than the level of noise so that the flaw response signal could be distinguished from the noise signal. Thus, the values used for the thresholds are $F_1^{th} = \mu_1 + 3\sigma_1 = 253.3317\ \Omega$ and $F_2^{th} = \mu_2 + 3\sigma_2 = 62.9078\ \mu T$.

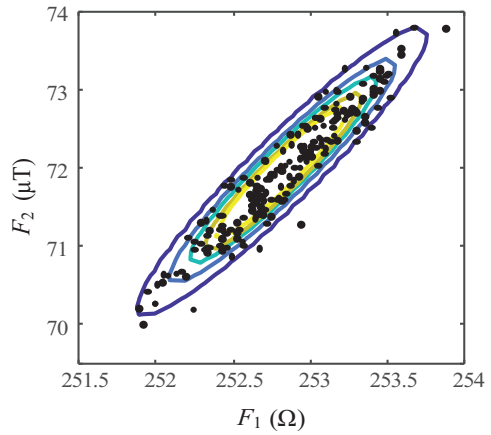

Fig. 10. Distribution of the response signal features.

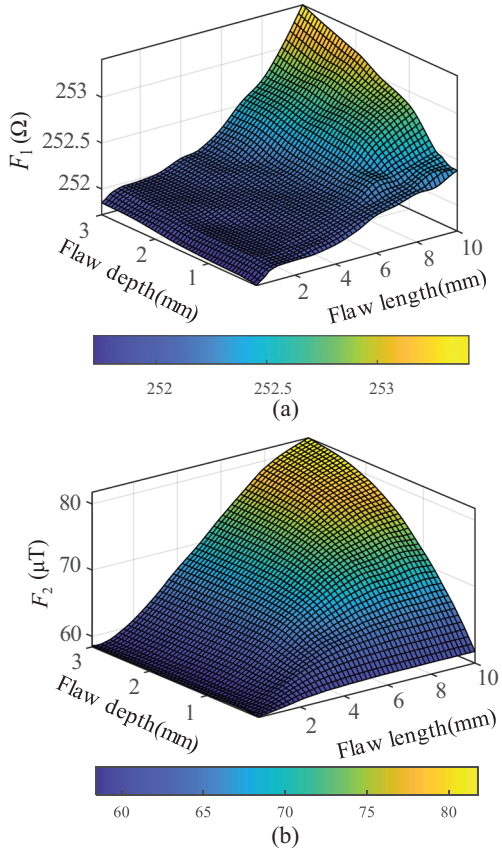

Fig. 11. Response signal features of the flaw regarding its length and depth: (a) F_1, and (b) F_2.

After determining the detection thresholds, the 2M-MAPOD is obtained in a discrete form based on equation (8). A continuous POD is finally obtained going through GLF regression and parameter optimization via the LM algorithm. The parameters are initialized as $\hat{\Theta}^0 =$ [1; 1; 1; 1; 1; 1; 1]. Two stopping criteria for the algorithm are set. One is the maximum number of iterations and the other is the error tolerance level. The maximum number of iterations is set to 5×10^4, and the tolerance level, representing the maximum difference of the residual sum of squares between two consecutive iterations ($\delta_k S(\Theta)$), is set to 1×10^{-5}. Eventually, the parameters estimated from the LM algorithm are $\hat{\Theta}$= [1.0, 1.7612, 1.5793, 1.2389, 2.4548, 0.3759, –0.7258]. From the estimated parameters $\hat{\Theta}$, the 2M-MAPOD model is acquired as shown in Fig. 14.

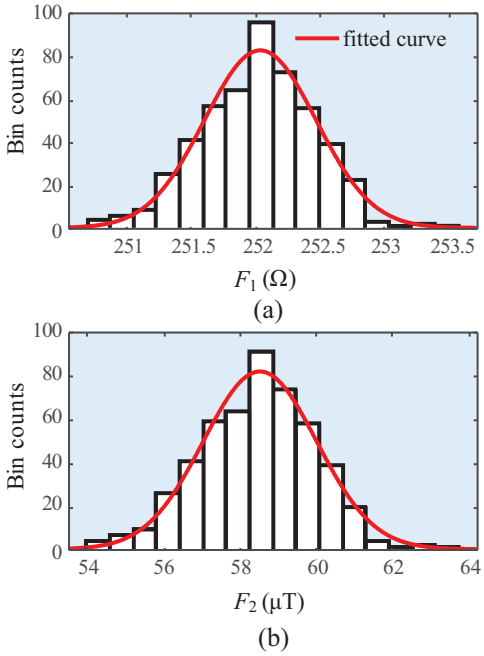

Fig. 12. Histogram plot of the noise distribution: (a) F_1 and (b) F_2.

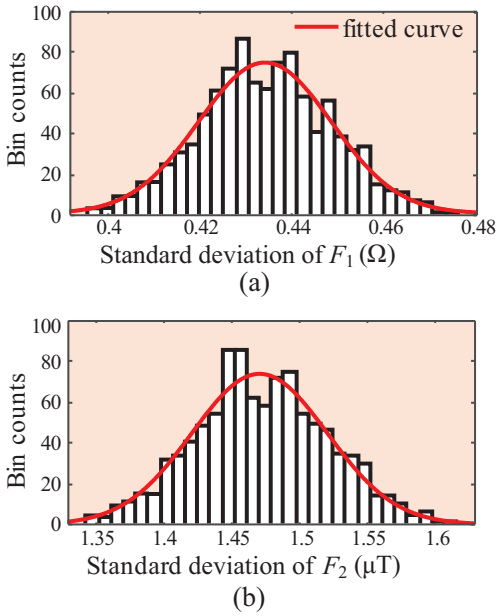

Fig. 13. Variation in the standard deviation of (a) F_1 and (b) F_2.

The black asterisks are the discrete POD obtained from equation (8), and the color surface is the continuous POD obtained by the GLF regression. In the POD analysis, it is crucial to include a confidence bound, as the estimated parameters are from a limited number of samples. However, it may not always be possible to increase the number of flaw parameters to construct the POD model. So, in order to encompass the confidence bounds, the bootstrap technique is applied. In our case, since 190 different flaw parameters are used to construct the 2M-MAPOD model, the confidence bounds are very narrow and hence not depicted.

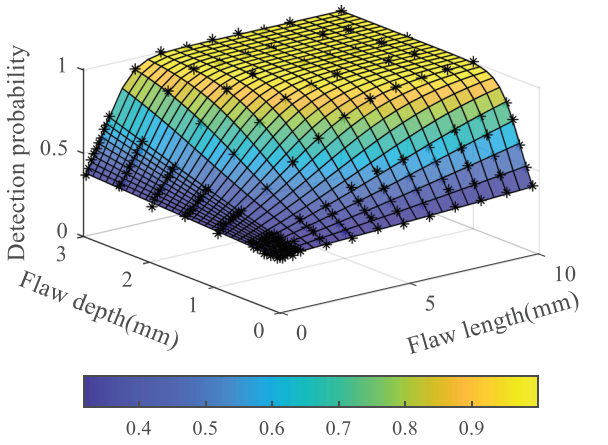

Fig. 14. Estimated 2M-MAPOD model.

IV. COMPARISON WITH TRADITIONAL POD ANALYSIS

A. COMPARISON WITH POD CONSIDERING SINGLE FLAW PARAMETER AND MULTIPLE RESPONSE SIGNALS

The results of proposed 2M-MAPOD are compared with POD considering single flaw parameter and multiple response signals. The single flaw parameter is either the flaw length or the depth. The flaw response signals remain the coil impedance and the magnetic flux density. The POD for each flaw length or depth is computed as:

$$Pod\left(F|L_{\text{flaw}} = L_i, D_{\text{flaw}} = Cons\right) = \int_{F_2^{\text{th}}}^{\infty}\int_{F_1^{\text{th}}}^{\infty} p\left(L_i, D_{\text{flaw}} = Cons\right)\mathrm{d}F_1\mathrm{d}F_2 \tag{12}$$

$$Pod\left(F|L_{\text{flaw}} = Constant, D_{\text{flaw}} = D_i\right) = \int_{F_2^{\text{th}}}^{\infty}\int_{F_1^{\text{th}}}^{\infty} p\left(L_{\text{flaw}} = Cons, D_i\right)\mathrm{d}F_1\mathrm{d}F_2 \tag{13}$$

POD considering single flaw parameter is 1-dimensional as the cross section of Fig. 14. As shown in Fig. 15, the blue line is the POD that only considers the flaw length with a fixed flaw depth of 1 mm and the red line is the POD that only considers the flaw depth with a fixed flaw length of 10 mm. POD considering two flaw parameters is 2-dimensional, allowing for a more comprehensive understanding of the relationship between the POD and these two flaw parameters than just single flaw parameter.

B. COMPARISON WITH POD CONSIDERING SINGLE RESPONSE SIGNAL AND MULTIPLE FLAW PARAMETERS

The results of proposed 2M-MAPOD are compared with POD considering single response signal and multiple flaw parameters. The single response signal is the coil impedance or the magnetic flux density. The flaw parameters remain the flaw length and flaw depth. The POD for each flaw response signal is computed as:

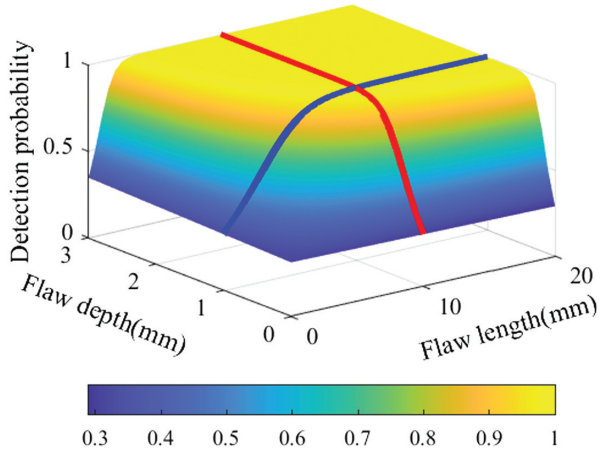

Fig. 15. POD considering two flaw parameters versus single flaw parameters.

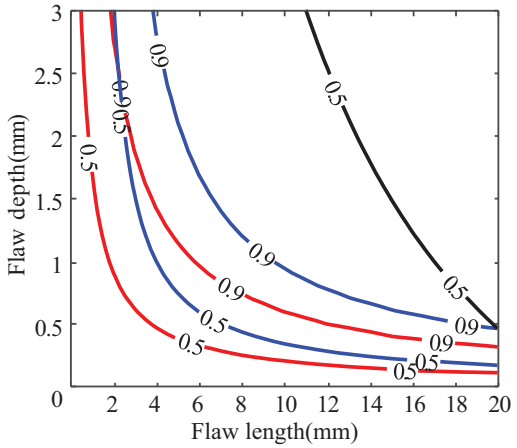

Fig. 16. POD analysis contours, red line: POD considering multiple response signals, blue line: POD only considering the magnetic flux density, black line: POD only considering the coil impedance.

$$Pod\left(F_1|L_{\text{flaw}}=L_i, D_{\text{flaw}}=D_j\right) = \int_{F_1^{\text{th}}}^{\infty} p\left(F_1|L_i, D_j\right)\mathrm{d}F_1 \tag{14}$$

$$Pod\left(F_2|L_{\text{flaw}}=L_i, D_{\text{flaw}}=D_j\right) = \int_{F_2^{\text{th}}}^{\infty} p\left(F_2|L_i, D_j\right)\mathrm{d}F_2 \tag{15}$$

The obtained POD contour plot is shown in Fig. 16. The red line represents the proposed 2M-MAPOD contours considering multiple response signals, the blue line represents the traditional POD contours considering the magnetic flux density with feature F_2, and the black line represents the traditional POD contours considering the coil impedance with feature F_1. The contour curves correspond to a_x of the relevant flaw parameters, where a_x is the $x\%$ probability that a flaw with a given parameter shall be detected. The a_{50} and a_{90} are plotted in Fig. 16. The proposed 2M-MAPOD contours are located at the lower left of the conventional ones, indicating that the proposed method still has a high detection probability for flaws with small parameters. To be specific, the proposed POD contour is 0.9, whereas the conventional POD contours are less than 0.9. The contour curves also indicate the presence of a correlation between the two flaw parameters. Longer and deeper flaws are easier to be detected.

C. COMPARISON WITH POD CONSIDERING SINGLE RESPONSE SIGNAL AND SINGLE FLAW PARAMETER

Traditional POD considering single response signal and single flaw parameter is calculated through the "$\hat{a}$ versus a" regression [33]:

$$\ln(\hat{a}) = A_0 + A_1\ln(a) + \varepsilon \tag{16}$$

where $\hat{a}$ could be the coil impedance or the magnetic flux density, while the single flaw parameter a is the flaw length or the flaw depth. A_0 and A_1 are coefficients to be estimated by the regression fitting. ε follows the distribution of $\mathrm{N}(0,\delta^2)$. With a defined threshold $\hat{a}_{\text{th}}$, which is also obtained from the noise condition based on 3σ criteria, the POD considering single response signal and single flaw parameter is computed as:

$$Pod(a) = 1 - \Phi\left(\frac{\ln(\hat{a}_{\text{th}}) - (A_0 + A_1\ln(a))}{\delta}\right) \tag{17}$$

where Φ is the standard normal distribution function.

Taking the relationship between the magnetic flux density F_2 and the flaw length as an example, the obtained "$\hat{a}$ versus a" plot is shown in Fig. 17. The flaw depth is fixed as 1 mm. The blue dots represent the measured values of F_2 for different flaw lengths at various lift-off distances. Normal curves and bar charts are distributed fits of the measured values. The brown line is a linear regression fitting of F_2 and flaw length. The red line is the decision threshold. The integral of the normal curve above the decision threshold is the POD value at the corresponding flaw length.

The calculated POD curve is plotted in Fig. 18, taking the flaw depth 1 mm (Fig. 18(a)) or the flaw length 10 mm (Fig. 18(b)) as examples. In Fig. 18(a), the red solid line

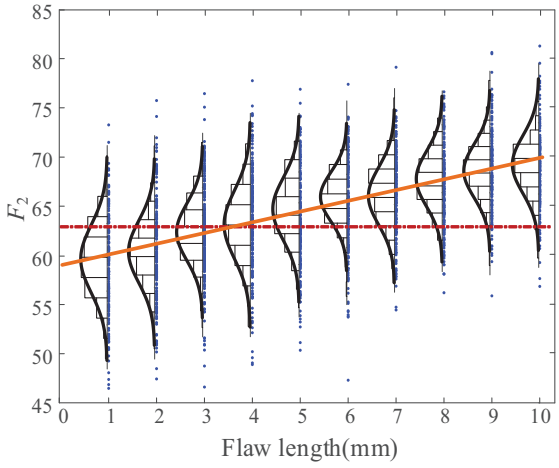

Fig. 17. "$\hat{a}$ versus a" plot showing the relationship between the magnetic flux density F_2 and the flaw length.

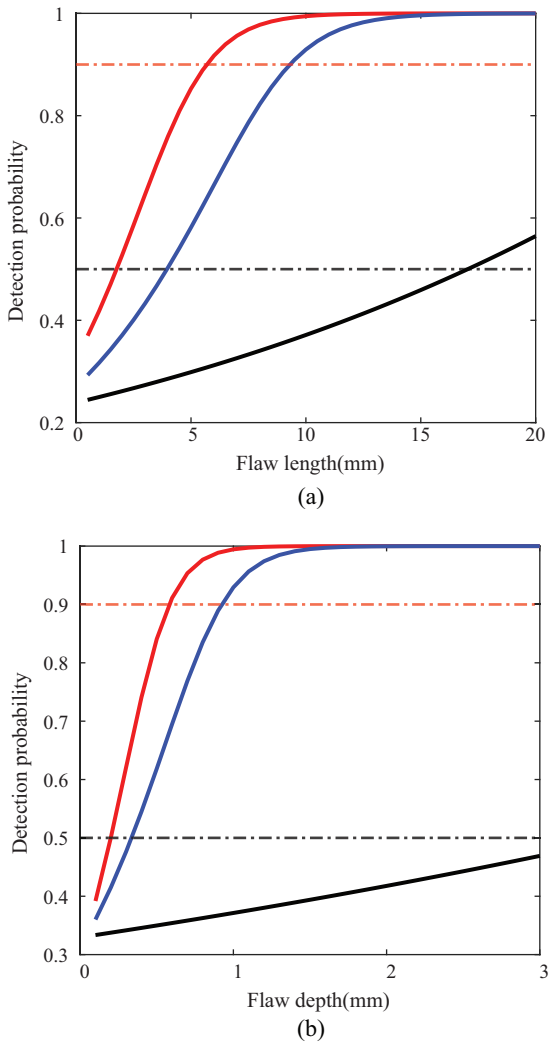

Fig. 18. Detection probability: (a) considering flaw length and (b) considering flaw depth, red solid line: POD considering multiple response signals, blue solid line: POD only considering the magnetic flux density, black solid line: POD only considering the coil impedance; red dashed line: $Pod = 0.9$, black dashed line: $Pod = 0.5$.

represents POD considering multiple signals and flaw length; the blue solid line represents POD only considering the magnetic flux density and flaw length; the black solid line represents POD only considering the coil impedance and flaw length; the red dashed line represents $Pod = 0.9$; and the black dashed line represents $Pod = 0.5$. In Fig. 18(b), the red solid line represents POD considering multiple signals and flaw depth; the blue solid line represents POD only considering the magnetic flux density and flaw depth; the black solid line represents POD only considering the coil impedance and flaw depth; and the red dashed line and the black line represent the same meaning as those in Fig. 18(a).

As shown in Fig. 18(a), the detection probability of single coil impedance signal is relatively lowest for all the flaw length with 17 mm flaw length still half possibility of misdetection. The magnetic flux density signal performs better than the coil impedance signal, meaning that magnetic flux density is more sensitive to the flaw during ECT than coil impedance. The minimum detectable length of 90% probability by the proposed 2M-MAPOD is 5.7 mm. a_{90} is 9.3 mm for single magnetic flux density signal, which means the detection results for flaw length smaller than 9.3 mm is not convincing. For the length of 5.7 mm, the detection probability using single magnetic flux density is only 64%. As shown in Fig. 18(b), the minimum detectable depth of 90% probability by the proposed 2M-MAPOD is 0.59 mm. a_{90} is 0.92 mm for single magnetic flux density signal. For flaw depth of 3 mm, the detection probability of single coil impedance signal is less than 50%. The integration of multiple response signals has better detection performance of ECT than single response signal.

V. CONCLUSIONS

In this paper, a 2M-MAPOD analysis is performed with consideration of multiple flaw parameters and multiple response signals to evaluate the detection reliability of ECT system. The multiple flaw parameters are the length and depth of a flaw. The response signals are the coil impedance and the magnetic flux density representing the electric and magnetic characteristics of the ECT system. A FEM is established to simulate multiple response signals under different flaw sizes and lift-off distances. The discrete POD is obtained by the FEM-assisted simulation data, and a GLF is created to obtain the continuous POD function. The applicability of the proposed 2M-MAPOD is evaluated for ECT against flaws on aluminum plates. For the flaw of 1 mm depth, the minimum flaw length of 90% detection probability considering multiple response signals is 5.7 mm, which is much smaller than single response signal. The proposed method performs well for a high detection reliability with small flaws.

The main limitation with this method is that a large dataset might be required to perform POD, which is time-consuming for three-dimensional FEM. In this paper, we have only taken into account defects with rectangular cross sections. Other geometries like semielliptic can also be studied because the flaw features also depend on its geometry. Also, we will further carry on more validation experiments and on-site application to use multiple response signals for flaw detection for the improvement of detection reliability.

ACKNOWLEDGMENTS

This work was supported by the Key Research and Development Project of Zhejiang Province (Grant No. 2023C01248, 2023C01069) and the National Natural Science Foundation of China (Grant No. 52375135, 52305137).

CONFLICT OF INTEREST STATEMENT

The authors declare no conflicts of interest.

REFERENCES

[1] F. Yu et al., "Receiver operating characteristic analysis for evaluating a proper experimental condition of eddy current tests under a low signal-to-noise ratio," *Int. J. Appl. Electromagn. Mech.*, vol. 71, pp. 179–189, 2023.

[2] E. Mohseni et al., "A study of the automated eddy current detection of cracks in steel plates," *J. Nondestr. Eval.*, vol. 39, p. 6, 2020.

[3] N. Yusa et al., "Evaluation of the electromagnetic characteristics of type 316L stainless steel welds from the viewpoint of eddy current inspections," *J. Nucl. Sci. Technol.*, vol. 51, no. 1, pp. 127–132, 2014.
[4] A. AbdAlla et al., "Challenges in improving the performance of eddy current testing: review," *Meas Control*, vol. 52, pp. 46–64, 2019.
[5] M. Bato et al., "Experimental and numerical methodology to obtain the probability of detection in eddy current NDT method," *NDT E Int.*, vol. 114, p. 102300, 2020.
[6] B. Yee et al., "*Assessment of NDE Reliability Data*," Cleveland, Ohio: NASA, 1976.
[7] G. Georgiou, "PoD curves, their derivation, applications and limitations". *Insight*, vol. 49, pp. 409–414, 2007.
[8] M. Sättele, M. Bründl, and D. Straub, "Reliability and effectiveness of early warning systems for natural hazards: concept and application to debris flow warning," *Reliab. Eng. Syst. Saf.*, vol. 142, pp. 192–202, 2015.
[9] R. Yan et al., "Study on the method of establishing the probability of detection curve for ultrasonic detection on railway hollow axle cracks," *Measurement*, vol. 224, p. 113866, 2024.
[10] M. Bajgholi et al., "Reliability assessment of non-destructive testing (NDT) for the inspection of weld joints in the hydroelectric turbine industry," *Int. J. Adv. Manuf. Technol.*, vol. 128, pp. 4223–4233, 2023.
[11] J. Knopp et al., "Considerations for statistical analysis of nondestructive evaluation data: hit/miss analysis," *E-J. Adv. Maint.*, vol. 4, no. 3, pp. 105–115, 2012.
[12] C. Annis, L. Gandossi, and O. Martin, "Optimal sample size for probability of detection curves," *Nucl. Eng. Des.*, vol. 262, pp. 98–105, 2013.
[13] R. Meyer et al., "*Review of Literature for Model Assisted Probability of Detection*," Richland, WA: Pacific Northwest National Laboratory, 2014.
[14] A. Rosell and G. Persson, "Model based capability assessment of an automated eddy current inspection procedure on flat surfaces," *Res. Nondestr. Eval.*, vol. 24, pp. 154–176, 2013.
[15] X. Du and L. Leifsson, "Efficient uncertainty propagation for MAPOD via polynomial chaos-based Kriging," *Engineering Computations*, vol. 37, pp. 73–92, 2019.
[16] K. Sun et al., "Model-based POD evaluation with parameters from experiment: a comparative study of TMR and coil array probes," *J. Nondestr. Eval.*, vol. 41, p. 27, 2022.
[17] B. Yang, "Modeling of eddy current NDT simulations by Kriging surrogate model," *Res. Nondestr. Eval.*, vol. 34, pp. 154–168, 2023.
[18] N. Yusa, W. Chen, and H. Hashizume, "Demonstration of probability of detection taking consideration of both the length and the depth of a flaw explicitly," *NDT E Int.*, vol. 81, pp. 1–8, 2016.
[19] M. Pavlović, K. Takahashi, and C. Müller, "Probability of detection as a function of multiple influencing parameters," *Insight*, vol. 54, pp. 606–611, 2012.
[20] N. Yusa and J. Knopp, "Evaluation of probability of detection (POD) studies with multiple explanatory variables," *J. Nucl. Sci. Technol.*, vol. 53, pp. 574–579, 2016.
[21] T. Tomizawa, Y. Guo, and N. Yusa, "Applicability of simulation-assisted probability of detection analysis considering multiple signal features to eddy current testing of weld," *Int. J. Appl. Electromagn. Mech.*, vol. 71, pp. 75–83, 2023.
[22] P. Baskaran et al., "Integration of multiple response signals into the probability of detection modelling in eddy current NDE of flaws." *NDT E Int.*, vol. 118, p. 102401, 2021.
[23] P. Baskaran et al., "Probability of detection modelling in eddy current NDE of flaws integrating multiple correlated variables," *NDT E Int.*, vol. 123, p. 102499, 2021.
[24] Z. Liu et al., "Multi-sensor cross-domain fault diagnosis method for leakage of ship pipeline valves," *Ocean Eng.*, vol. 299, p. 117211, 2024.
[25] X. Li et al., "Multi-sensor fusion fault diagnosis method of wind turbine bearing based on adaptive convergent viewable neural networks," *Reliab. Engineering Syst. Saf.*, vol. 245, p. 109980. 2024.
[26] O. Biro and K. Preis, "On the use of the magnetic vector potential in the finite-element analysis of three-dimensional eddy currents," *IEEE Trans. Magn.*, vol. 25, pp. 3145–3159, 1989.
[27] Z. Zeng et al., "Reduced magnetic vector potential formulation in the finite element analysis of eddy current nondestructive Testing," *IEEE Trans. Magn.*, vol. 45, pp. 964–967, 2009.
[28] H. Zhou et al., "Study on the optimization of eddy current testing coil and the defect detection sensitivity." *14th Int. Conf. Pressure Vessel Technol.*, vol. 130, pp. 1649–1657, 2015.
[29] A. Brown and C. Eviston, "Model development and validation of geometrically complex eddy current coils using finite element methods," *43rd Annu Rev. Prog Quant. Nondestructive Evaluation*, vol. 1806, p. 110015, 2017.
[30] C. Reboud et al., "Statistical study of ECT detection around fasteners using simulation based POD curves," *CP1211, Rev. Quant. Nondestructive Evaluation*, vol. 1211, pp. 1903–1910, 2010.
[31] A. Kankainen, S. Taskinen, and H. Oja, "On Mardia's tests of multinormality," In *Theory and Applications of Recent Robust Methods*. Basel: Birkhäuser, 2004, pp. 153–164.
[32] K. Madsen, H. Nielsen, and O. Tingleff, "Methods for nonlinear least squares problems," pp. 24–30, 2004.
[33] G. Lv, S. Guo, D. Chen et al., "Laser ultrasonics and machine learning for automatic defect detection in metallic components," *NDT & E Int.*, vol. 133, p. 102752, 2023.